Templated synthesis of nanostructured europium-doped yttrium oxide thin films

ANTHONY Y. KU*, WILLIAM J. HEWARD, VANITA MANI
General Electric, Global Research, Niskayuna, NY 12309, USA
E-mail: kua@research.ge.com

Published online: 28 March 2006

An evaporation-assisted templating method was developed for the synthesis of nanostructured europium-doped yttrium oxide (Y_2O_3:Eu^{3+}, YEO) thin films. The method involves spin-coating a solution containing yttrium salt and block copolymer followed by thermal oxidation. Uniform films with controllable thickness ranging from 100 to 500 nm were obtained by tuning the composition of the precursor solution and the processing conditions. However, the method was not completely general as extremes in salt or polymer concentration triggered uncontrolled cracking and texturing of the film. The photoluminescence was proportional to both the thickness and surface roughness. Nanocrystalline, porous YEO particles produced using the evaporation method exhibited an intrinsic quantum efficiency approximately 25% of that of particles with micron-sized crystallites. © *2006 Springer Science + Business Media, Inc..*

1. Introduction

Europium-doped yttria (Y_2O_3:Eu^{3+}, YEO) is used commercially as a red phosphor because of its high quantum efficiency (QE) and good stability [1]. In recent years, there has been interest in YEO nanoparticles and thin films for low voltage cathodoluminescent devices. Although YEO nanoparticles and thin films exhibit reduced QE and overall brightness relative to micron-sized particles [2, 3], they are still of interest because these disadvantages are offset by the stability, potential for higher packing densities, and high lateral resolutions that may be possible. Furthermore, the brightness of nanocrystalline thin films can be improved by coating them on textured substrates which reduces the internal reflections from the YEO film surface [4–6].

Presently, methods for preparing YEO nanoparticles and thin films can be grouped into two broad categories: vapor deposition and wet chemistry methods. Vapor deposition methods, such as chemical or physical vapor deposition, can be used to produce either particles or thin films. They allow reasonable control over the stoichiometry and particle size or film thickness, but generally require extreme conditions and are limited in batch size [2–11]. Wet chemistry methods generally involve the precipitation of the material from solution, followed by a heat treatment to convert the precipitate into a crystalline oxide [12–17]. In many cases, a templating agent is used to control the morphology of the resulting particles. Nanoparticles or nanotubes are produced when the templating agent encapsulates the growing deposit [13, 16]. Alternately, the template can be encapsulated within the precipitate leading to mesoporous particles [18]. This porosity impacts the luminescence properties through the microstructure [17]. While wet chemistry approaches are less expensive than vapor deposition approaches, they require an intermediate consolidation or heating step. This makes it difficult to obtain uniform, nanocrystalline thin films due to morphological changes during the post deposition treatment.

In this report, a direct wet chemistry method for preparing nanostructured YEO thin films is described. The method involves spin-coating an ethanolic precursor solution containing yttrium and europium salts and a block copolymer template, followed by heating in air. Similar approaches have been used previously in the synthesis of thin films of mesoporous metal oxides of silica, titania, and zirconia [19, 20]. Here, the key synthesis conditions for structural control of YEO films are identified. The apparent brightness of the films could be increased using rough substrates. This approach was also used to produce nanocrystalline porous YEO particles to evaluate the intrinsic QE relative to particles with larger crystallite size.

2. Experimental procedure

2.1. Synthesis

YEO thin films were prepared from a solution containing yttrium and europium salts and a nonionic block copolymer templating agent in ethanol. The templating agent also acted as a wetting agent in the thin film synthesis. The

*Author to whom all correspondence should be addressed.
0022-2461 © *2006 Springer Science + Business Media, Inc..*
DOI: 10.1007/s10853-006-6769-3

concentrations of the block copolymer (0 to 15% wt.) and salt (0.5 to 55% wt.) were varied to map the experimental phase space. Since intimate mixing of the Y^{3+} and Eu^{3+} ions occurs during the synthesis, the europium dopant level was controlled by adjusting the stoichiometry in the precursor solution through the relative amounts of europium and yttrium salts. In this work, the doping level was held constant at 5% wt. Eu. In a typical synthesis, the block copolymer ($EO_{106}PO_{70}EO_{106}$, Pluronic F127, BASF) was dissolved in 10 g of ethanol. Yttrium nitrate hydrate ($Y(NO_3)_3 \cdot 6H_2O$) and europium nitrate hydrate ($Eu(NO_3)_3 \cdot 5H_2O$) were added with stirring for 30 min to completely dissolve the salts.

Thin films were prepared by spin-coating the precursor solution onto three types of substrates: bare *n*-type silicon wafers (Si), aluminum-coated *n*-type silicon wafers (Al–Si), and porous anodic alumina supported on n-type silicon wafers (AAO–Si) [21]. The different roughness of these substrates provided insight into the effects of surface roughness on the brightness of the YEO emission. The aluminum-coated substrates were prepared by sputter-depositing a 1 μm layer of aluminum onto 100 mm Si wafer. The nanoporous anodized aluminum oxide (AAO–Si) coated Si wafers were prepared by electrochemically oxidizing the aluminum layer at the constant voltage of 40 VDC in 0.3 M oxalic acid at 20°C for ~350 s. At 40 VDC, the current density is approximately 7–8 mA/cm^2. The resulting 1.2 μm AAO films were rinsed in deionized water and dried in air.

Films were prepared by depositing about 1 mL of precursor solution onto the substrates, followed by spinning at a constant rate from 500 to 5000 rpm for 60 s. The samples were then aged for 30 min, and calcinated in air at 600°C for 4 h to convert the block copolymer-salt deposit into the oxide. The films were heated at 60°C/h and cooled at 300°C/h. Thermogravimetric analysis (TGA) and differential thermal analysis (DTA) were used to study the structural evolution during the thermal treatment. The thickness and surface roughness of the calcined samples was measured using ellipsometry and optical profilometry. In addition, some samples were randomly selected for scanning electron microscopy (SEM) and x-ray diffraction (XRD) analysis to validate the thickness measurements and confirm the mesoporosity and crystallinity of the yttria host structure.

Nanostructured particles were prepared by evaporating the precursor solution in an open Petri dish at room temperature. A gel was formed by complete evaporation of the ethanol within 1–7 days. Calcination of the gel in air at 600°C or 1000°C for 4 h resulted in particulate YEO. The particles were examined using SEM and XRD. Nitrogen adsorption-desorption isotherms of the structure were collected to evaluate the porosity of the particles.

2.2. Characterization

TGA and DTA data was collected using a NETZSCH Model 409 Simultaneous Thermal Analysis system. Gelled samples were heated to 700°C at a rate of 1°C/min. Control measurements were performed on the template and the yttrium nitrate salt.

XRD was used to determine the crystallinity and phase of the YEO. Scattering patterns were recorded for the calcined thin film, the gel after evaporation, and the calcined powder. High angle (10–90° 2θ) diffraction patterns were collected using a θ-θ Bruker D8 Advance diffractometer equipped with a linear position-sensitive detector (PSD-50 m) manufactured by M. Braun. Nickel-filtered copper Kα radiation was used with an aperture slit of 0.6 mm. NIST-certified SRM 660a LaB_6 was used to determine the instrumental contributions to the diffraction peak broadening. Low angle diffraction data was performed on the calcined materials to check for ordered porosity due to the block polymer template. Data was collected on a θ-2θ Bruker D8 diffractometer using copper Kα radiation and a NaI(Tl) scintillation detector. Step scans were performed from 0.75–10° 2θ with aperture and scattered radiation slits of 0.6 mm and a detector slit of 0.05 mm and a 5 s count time.

High resolution SEM (HR-SEM) analysis of the films was performed in a Hitachi model S-4500 FE SEM equipped with a PGT PRISM digital EDS X-ray detector and IMIX analysis system using a beam energy of 5 kV. The samples were prepared by mounting them onto aluminum stubs using conductive carbon tape and paste. A thin coating of Pt was sputtered onto the membranes to reduce charging.

The thickness and index of refraction of uniform thin films on silicon wafer substrates were measured using a Woollam M2000UI spectroscopic ellipsometer. The thickness was obtained by averaging measurements from 2–5 regions on a given sample. The sample size for each measurement was an ellipse with a minor radius of 3 mm. The thickness and index of refraction of the film were fitted using a one-layer Cauchy model for the dependence of the index of refraction on wavelength [22]. The fitted thickness agreed with HR-SEM measurements to within 5%.

The surface roughness was measured using a MicroXAM surface mapping microscope equipped with a Phase Shift Technology optical profilometer. Optical profilometry was used instead of atomic force microscopy (AFM) because of its higher throughput and larger sampling area (5 mm × 4 mm). The RMS roughness was automatically computed by the imaging system (Mapvue software).

Nitrogen adsorption-desorption measurements were performed using a Micromeretics ASAP2020 system. Samples were loaded into the sample cell, degassed overnight at 70°C before loading into the instrument. Nitrogen adsorption and desorption measurements were collected from 0.05 to 0.995 P/P_0 relative pressure. The surface area was estimated using the Brunauer-Emmett-Teller (BET) model.

Photoluminescence measurements were performed using a SPEX 1680 double-monochrometer UV-vis

spectrometer. Emission spectra ($\lambda_{ex} = 254$ nm, 550 to 700 nm) from the samples were collected in reflectance mode using an excitation wavelength of 254 nm. For the nanostructured particles, powder plaques were prepared. The quantum efficiency of the particles relative to a commercially available YEO phosphor (GE Global Standard YEO, GS-YEO) is given by [23]:

$$QE_{\text{sample/std}} = \frac{\text{Int Area}_{\text{sample}}}{\text{Int Area}_{\text{std}}} \cdot \frac{\text{Abs}_{\text{std}}}{\text{Abs}_{\text{sample}}} \qquad (1)$$

where Int Area$_i$ is the integrated intensity of the spectrum from sample i and Abs$_i$ is the absorbance of sample i. The absorbance was measured relative to a $BaSO_4$ plaque and is given by:

$$\text{Abs} = 1 - 0.952\left(\frac{I_{\text{sample}}}{I_{\text{BaSO}_4}}\right) \qquad (2)$$

where I_i is the measured intensity at 254 nm for sample i illuminated at 254 nm.

3. Results

3.1. Thin Films

The as-spun films on silicon wafers were initially uniform with a slight color that varied with the film thickness. Fig. 1 is a composition-morphology diagram for the samples after 30 min of aging. Uniform thin films were obtained over a limited range of polymer and salt concentration. It is well known in the literature that the thickness of a spin-coated layer varies as the spin rate to the negative two-thirds power [24]. Regression of the ellipsometric thickness data confirmed this dependence for the uniform films. Two types of inhomogeneities were encountered at extremes of polymer and salt concentrations. At polymer concentrations above about 10% wt., the film developed radially symmetric crystalline domains reminiscent of spherulites. Fan-like crystalline domains similar to those observed in smectic liquid crystalline films appeared at nitrate salt concentrations above about 20% wt. Both types of inhomogeneities were present at high polymer and salt concentrations. Near the phase boundaries, some samples developed inhomogeneities while other samples remained uniform. The differences in behavior were due to slight variations in the processing conditions. Immediately after spin-coating, all of the samples were visually uniform. At high polymer or salt concentration, inhomogeneities

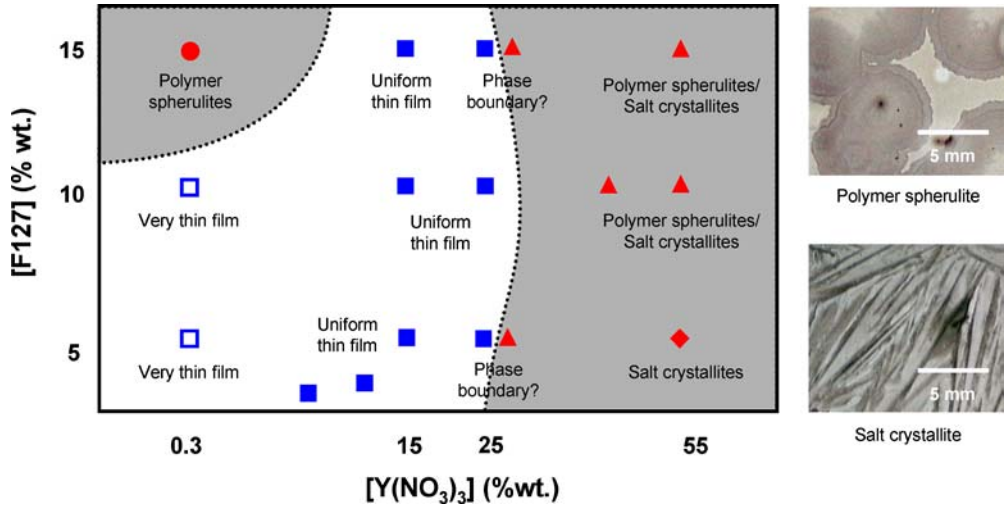

Figure 1 Composition-morphology diagram of thin film structure 30 min after spin coating. Uniform thin films (blue squares) were obtained over an intermediate range of polymer and yttrium salt concentrations. Extremes in polymer and salt concentration led to polymer spherulites (red circle, triangle) and/or salt crystallites (red diamond, triangle). Optical micrographs of the polymer spherulites (right, top) and salt crystallites (right, bottom) show the distinct morphologies associated with each structure.

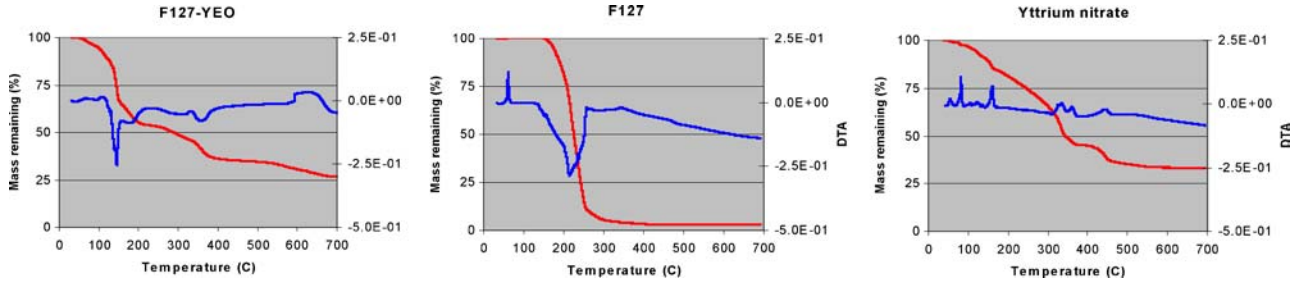

Figure 2 Thermal evolution of the sample. TGA and DTA plots for (a) F127-nitrate salt, (b) F127 template, and (c) yttrium nitrate salt.

TABLE I. Morphology of films prepared on Si, AAO-Si and Al-Sis

Sample	Spin rate (rpm)	Thickness (nm)	RMS roughness (nm)	UV-PL (a.u.) [$\lambda = 612$ nm]
Si	3000	275	53	3.1×10^5
	1000	475	66	6.4×10^5
Al	3000	280	1260	11.1×10^5
AAO	3000	240	17	3.7×10^5
	1000	450	20	8.2×10^5

nucleated at the edge of the substrate and spread over the entire film within a few minutes after spin-coating. For samples with compositions near the phase boundary, the onset of crystallite or spherulite growth did not begin for a few hours. Non-uniform films were obtained after calcination of as-prepared samples with spherulites or crystallites.

Fig. 2 shows the thermal evolution of the gelled material as it is heated. The TGA data shows a sharp loss of about 15% at 150°C, followed by the gradual loss of an additional 30% up to 400°C. The DTA plot shows a narrow exothermic event around 150°C and several less events at higher temperatures. TGA and DTA data for the constituent components of the gel are also shown. The template alone completely burns out between 175 and 250°C. The burnout is accompanied by a broad exothermic peak in the DTA plot. In contrast, the nitrate salt data shows a gradual loss of mass through 400°C, accompanied by several endothermic peaks.

Detailed characterization was performed on films prepared using compositions in the uniform region of the composition-morphology diagram. Table I lists the thickness and roughness of films prepared on the three different substrates using a single composition ([F127] = 10% wt, $[Y(NO_3)_3] = 23\%$). The films prepared on Si and AAO-Si substrates remained visually uniform after heat treatment. In contrast, films prepared on the Al–Si substrates developed a cloudy appearance. Fig. 3 shows cross-sectional HR-SEM images of the YEO films. The thickness of the YEO film is spatially uniform and comparable between the substrates for a fixed spin rate. As expected, the thickness increased when the spin rate was reduced. A slight texturing of the films, suggestive of nanometer level porosity, was also observed. Examination of the Al–Si sample revealed coarsening of the Al layer. This "hillocking" effect is well-known in the semiconductor industry and occurs around 300°C [25]. The cloudy appearance of the film on the Al-Si substrate can be explained by hillocking of the Al during calcination. Detailed examination of the YEO film coated onto the AAO-Si substrate revealed partial filling of the AAO pores by YEO.

XRD analysis of the samples confirmed that the calcined films contained a crystalline yttria host matrix in all cases. Typical XRD patterns for YEO samples prepared on Si substrates are shown in Fig. 4. The crystallite size was inferred from the breadths of the XRD peaks. Williamson-Hall analysis was used to separate the peak broadening effects of crystallite size from non-uniform lattice strain [26]. This approach involved plotting $\beta \cos\theta$ vs. $4^* \sin\theta$, where β is the instrument corrected peak broadening in

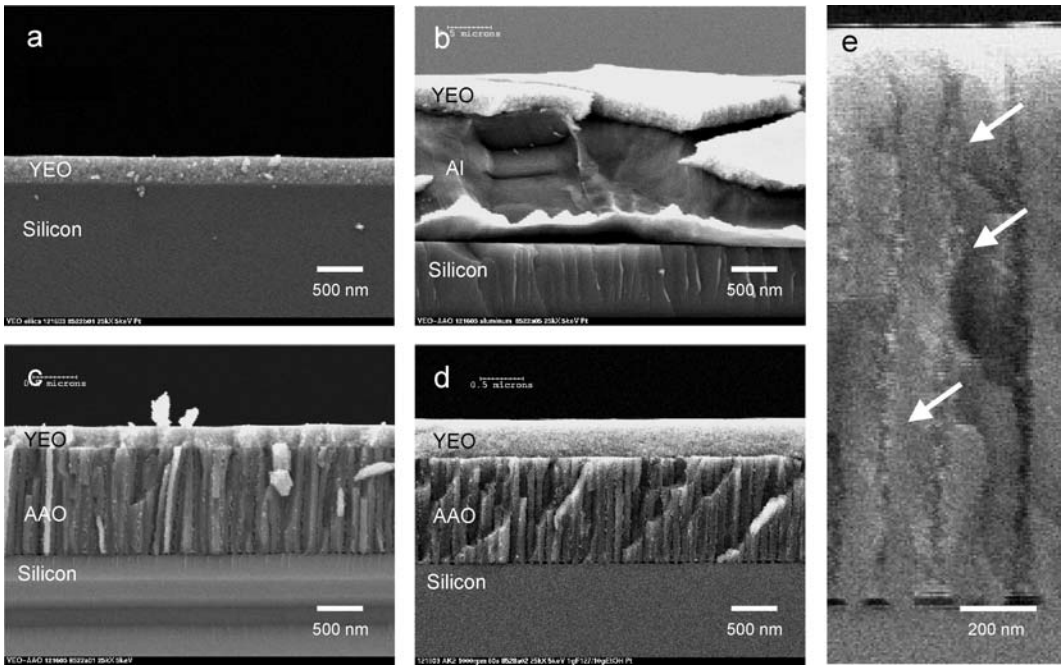

Figure 3 HR-SEM cross-sectional images of YEO thin films on Si (a), Al (b), and AAO (c-e) substrates. YEO films were prepared by spin-coating a 10% wt. F127 and 20% wt. $Y(NO_3)_3$ ethanolic solution at 3000 rpm (a-c) and 1000 rpm (d,e). The film on Si is a benchmark for comparison. Films prepared on Al (b) and AAO (c) under identical conditions are comparable in structure and thickness. Nanoparticles appear as light colored dots in the pores of the AAO (c-e) and are indicated by the white arrows (e). As expected, the film prepared at a lower spin rate (d) is noticeably thicker than its counterpart (c).

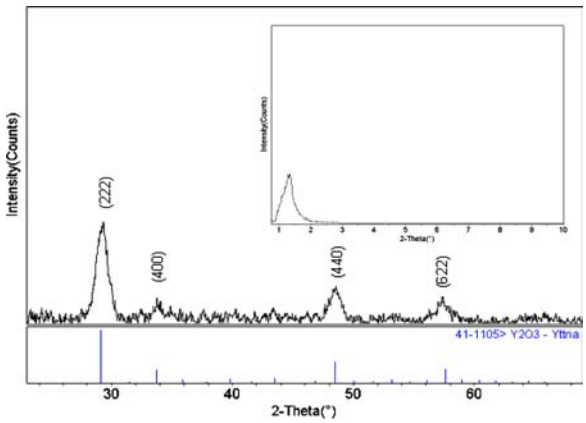

Figure 4 XRD data for thin films on Si wafer. The sample was prepared by spin-coating a 10% wt. F127-ethanol solution, 23% wt. $Y(NO_3)_3$ solution onto a silicon wafer at 3000 rpm followed by annealing at 600°C for 4 h in air. The peak broadening is indicative of ∼ 9 nm nanocrystallites. Inset: A peak corresponding to mesoporous channels with ∼6 to 8 nm periodicity appears in the small angle x-ray trace.

radians. If the data fall on a straight line, the size and strain are similar in each crystallographic direction and a spherical crystallite can be assumed. The crystallite size and strain can then be computed from the intercept and slope of the line. Crystallite sizes for the YEO films were ∼9 nm. Generally only four peaks were intense enough to profile in the thin film samples, and the results were indicative of isotropic properties. The Scherrer equation, which ignores contributions from strain, yielded similar size results. Low angle XRD analysis of the films revealed mesoscopic order with a characteristic spacing between 6 and 8 nm. In mesoporous materials, this corresponds to the porosity formed by the polymer template. The d-spacing is slightly smaller than that reported for mesoporous silica prepared using the same template ($d \sim 11$ nm) [27]. However, this may be due to the different local environment near the block copolymer in the gel. We also noted the absence of higher order peaks which suggests that the porosity consists of disordered channels.

Fig. 5 shows a typical emission spectrum from a YEO thin film. The primary emission peak corresponds to the $^5D_0 \rightarrow {}^7F_2$ electronic transition and is centered around 612 nm [1]. The intensity of the primary peak for each sample along with its thickness of the film, its surface roughness and peak intensity at 612 nm are listed in Table I. The peak intensity appears to increase with film thickness and surface roughness. Absorption of the exciting and emitted light was ignored because the all of the films were thinner than the penetration depth ($\sim 1\ \mu$m) of the exciting and emitted light.

3.2. Particles

Evaporation of the precursor solution resulted in transparent gels with a slight yellowish-brown color. The precursor gel oxidized during calcination to produce a fluffy white powder. The structural and luminescence properties of the particles are summarized in Table II. XRD analysis of the samples confirmed that the product was YEO in all cases.

Fig. 6 shows XRD patterns from the sample before and after calcination. The as-prepared gel produced peaks consistent with yttrium nitrate hydrate. Severe texturing was noticed in the diffraction pattern, which is a result

TABLE II. Summary of experimental results

Sample	XRD crystallite size (nm)	BET SA (m^2/g)	Relative QE (%)
GS-YEO	>100 nm	1.6	100
600 C/4 h	9	49	21.0
1000 C/4 h	35	19	27.8

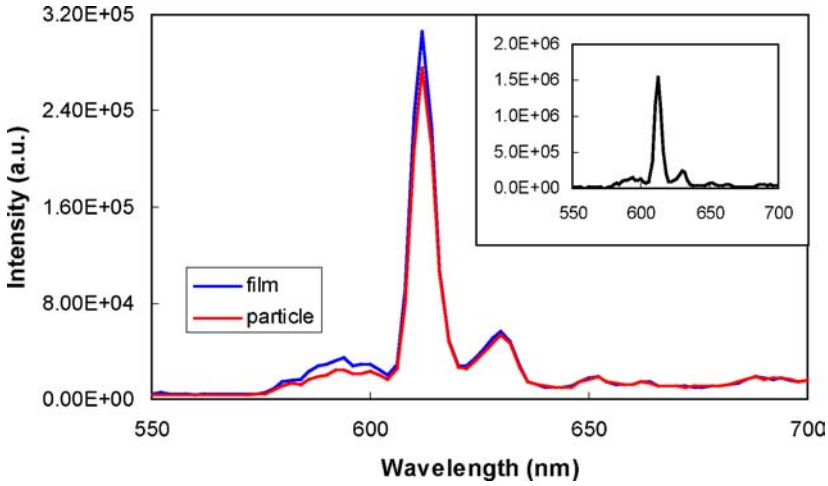

Figure 5 UV-PL data ($\lambda_{ex} = 254$ nm) for a YEO (5% wt Eu) synthesized from an ethanol-based salt-polymer precursor. The plot shows photoluminescence spectra for (a) a 275 nm thick film and (b) nanocrystalline porous particles. The film was prepared by spin-coating a 10% wt. F127, 23% wt. $Y(NO_3)_3$ ethanol solution onto a silicon wafer at 3000 rpm followed by annealing at 600°C for 4 h in air. The particles were prepared by evaporating the ethanol and firing the residue under the same conditions. Inset: The UV-PL spectrum for GS-YEO particles exhibits similar emission peaks, but the intensity of the emission is greater by a factor of 4.

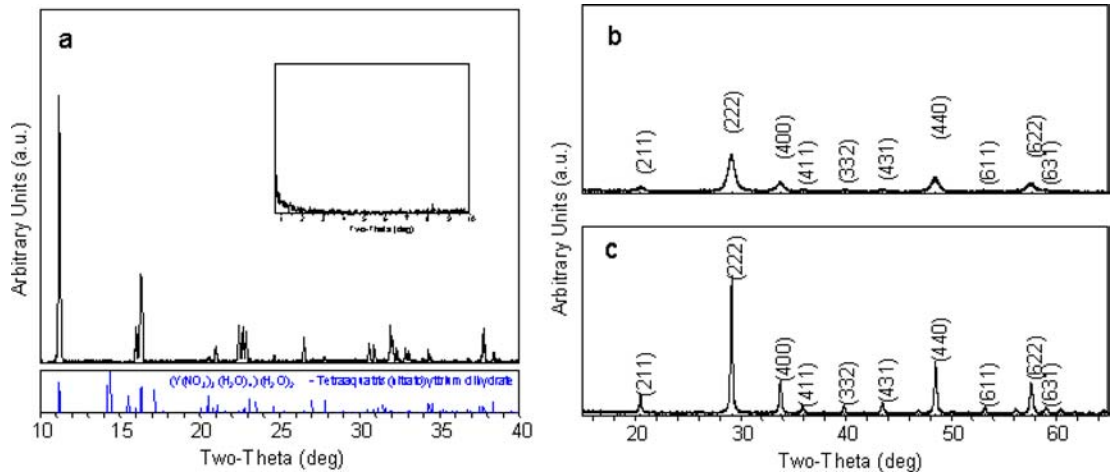

Figure 6 XRD of (a) as-prepared gel formed from yttrium nitrate and europium nitrate and YEO after calcination at (b) 600°C and (c) 1000°C. The peaks become sharper with increasing temperature indicating growth of the nanocrystallites from 9 nm to 35 nm. Inset: Small angle XRD pattern. No small angle peaks are present indicating a lack of organized mesoscopic structure due to the surfactant. Indices for the peaks in (a) are available as Electronic Supplementary Material.

of insufficient grinding of the macroscopic crystals. After calcination, only peaks corresponding to yttria were observed. No small angle peaks were observed in any of the gel samples suggesting that the mesoscopic ordering of the polymer did not occur. In experiments performed at higher temperatures, macroscopic crystals formed in addition to the gel. The formation of crystals at higher temperatures, where the evaporation rate is more rapid, provides further evidence that the gelation process is driven by the solubility of the yttrium salt as the solvent evaporates. It is likely that the polymer was completely excluded from the growing crystal in these cases.

The crystallite size in the calcined particles was inferred from the breadths of the XRD peaks using Williamson-Hall analysis. Crystallite sizes for the YEO powders ranged from 9 nm to 35 nm, increasing with calcination temperature. Similar to the thin film YEO, no significant amount of strain was seen in any of the samples. Some porosity is present as BET surface area measurements revealed specific surface areas ranging from 13.1 to 48.8 m^2/g as compared to 1.6 m^2/g for fully dense GS-YEO. Pore coalescence and other effects associated with sintering may explain the decrease in surface area with increasing calcination temperature [28]. The nitrogen adsorption results, coupled with the absence of small angle peaks in the XRD confirm that organized mesoporosity is not present in the particles.

Fig. 7 shows SEM images of the particles after calcination. A branched network morphology is present with perforations along the structure. The particles are on the order of a hundred microns in size. The branches appear to consist of nanocrystalline agglomerates. Coarsening of the structure through thickening of the branches and loss of perforations is observed in samples calcined at 1000°C. This is consistent with the trend in XRD crystallite sizes in Table II.

Strong red emission is observed from the powder upon illumination by UV ($\lambda_{ex} = 254$ nm) light. The computed quantum efficiency ranges from about 21 to 28% relative to GS-YEO. As seen in Fig. 5, the UV-PL intensity for particles heated to 600°C is comparable to that of 275 nm thick films and about a quarter that of the GS-YEO. None of the as-prepared gels exhibited luminescence under UV ($\lambda = 254$ nm) illumination.

4. Discussion

4.1. Templated synthesis

The templated synthesis scheme developed in this work is a two-step process in which a salt and block copolymer deposit is formed by evaporation and subsequently converted into a mesoporous oxide by heating in air. To a first approximation, the mesostructure results from organization of the block copolymer into a liquid crystalline phase during the evaporation with the salt partitioning into the hydrophilic phase of the liquid crystalline structure. The behavior seen in Fig. 1 indicates that, in the case of yttrium salts, the formation of a uniform film only occurs over a limited region in the composition space. Excess quantities of either salt or polymer leads to macroscopic phase separation and the subsequent formation of salt crystallites or polymer spherulites.

Salt crystallite formation can be understood in terms of the salt and polymer solubilities and the rate of evaporation. For the thin films, the rapid evaporation of solvent leads to viscous polymer-salt deposits. This deposit is metastable in cases where the salt concentration exceeds the solubility limit in the polymer. However, the kinetics of crystallite formation are hindered by the viscosity of the deposit. Crystallite nucleation and growth, when it did occur, invariably began at the edge of the substrate where the deposit was thickest. A similar line of reasoning can

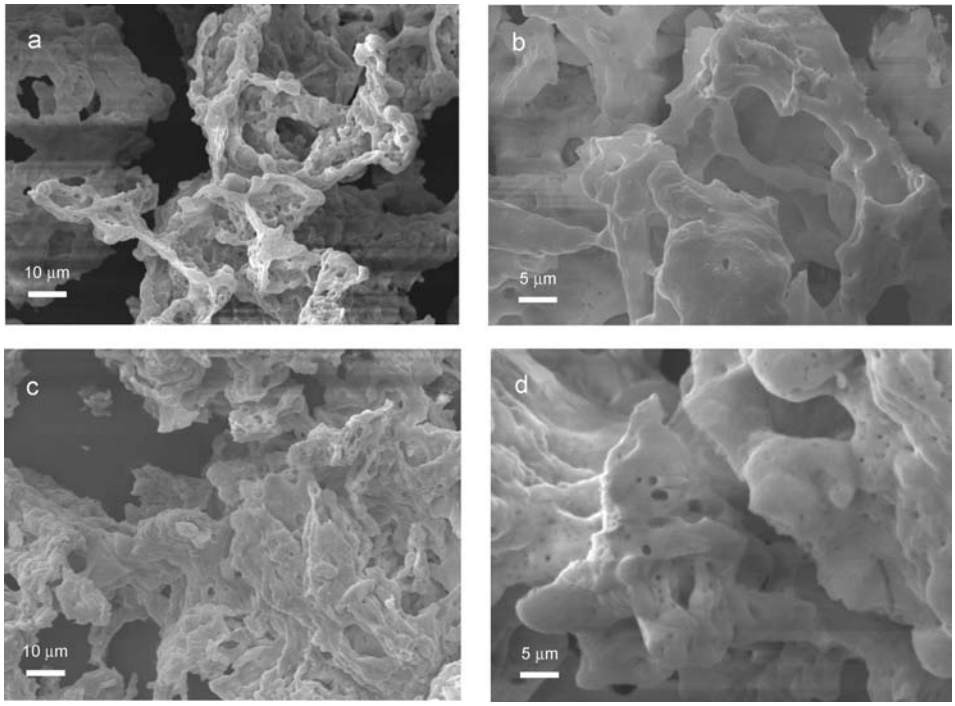

Figure 7 SEM images of YEO calcined at (a, b) 600°C and (c, d) 1000°C. The samples were prepared from a 10% wt. F127, 23% wt. $Y(NO_3)_3$ ethanol solution and heated for 4 h in air.

be applied to spherulite formation. At room temperature, Pluronic F127 forms a liquid crystalline phase between about 20 and 85% wt. in water [29]. Deposits with salt to polymer ratios in this range are expected to remain structurally uniform. However, at concentrations above 85% wt., F127 crystallizes. This explains the tendency for spherulite formation in compositions containing high polymer and low salt concentrations. The simultaneous formation of spherulites and salt crystallites at high polymer and salt concentrations suggests that macroscopic phase separation of the deposit into polymer and salt rich regions may be occurring. For the particles, the relatively slow evaporation of the ethanol led to faceted macroscopic crystals of yttrium nitrate hydrate. The exclusion of polymer from the salt crystal explains the lack of mesoporous structure in the particles after conversion to the oxide.

Two changes occur upon heating. The block copolymer template is burned out and the salt oxidizes to form yttria. The TGA and DTA data in Fig. 2 suggest that these events begin around 150°C, with the burnout of the template. Oxidation of the salt begins at about 160°C, resulting in a porous superstructure in which the space occupied by the template is preserved. The stresses associated with the conversion yttrium nitrate hydrate ($\rho \sim 2.68$ g/cc) to yttria ($\rho \sim 5.01$ g/cc) are relatively small due to the close match between the volumetric densities of yttrium [30]. However, excessive ramp rates can lead to pressure gradients due to gas evolution due to template burnout that may disrupt the structure. Elevated heating temperatures also cause nanocrystallite growth (Table II) leading to the loss of the mesoporosity.

Further insight into the structural evolution of the thin film during its conversion to the oxide was obtained through ellipsometry measurements of the index of refraction. Since the as-prepared films contained varying amounts of polymer, it was possible that the YEO films had differing degrees of porosity. If this were the case, the index of refraction would vary with the density. However, the constancy of index of refraction across all samples ($n = 1.7 \pm 0.09$) suggested that the film densification during polymer decomposition produced films with comparable density and index.

4.2. Films on AAO

On AAO, the film formed an overlayer which covered the pore openings. This overlayer was slightly thinner than a film prepared on a flat substrate under similar conditions (245 nm vs. 275 nm for 3000 rpm and 450 nm vs. 475 nm for 1000 rpm) suggesting that the film was either more dense than its thin film counterpart or that less material was present in the initial deposit. The first possibility is unlikely given the tendency of thin films to densify to a consistent level for a given thermal treatment. This was seen in the flat substrates where similar indices of refraction for measured a wide range of deposit composition. Instead, the thinner overlayer is more likely due to infiltration of the precursor solution into the AAO pores during the spin-coating process.

During spin-coating, centrifugal forces drive outward radial fluid flow. At the same time, evaporation of the solvent increases the viscosity of the solution, reducing the

flow rate. The thickness of the deposit is determined by the competition between these effects. For a given spin rate, faster evaporation can lead to a thicker deposit as less of the precursor solution is spun off the substrate. The ethanol in the AAO pores acts as a reservoir effectively reducing the evaporation rate relative to films coated on a flat substrate. This allows the loss of more mass to centrifugal flow and, ultimately, a thinner overlayer. A side effect of this process is the nucleation and growth of deposit nanoparticles in the AAO pores as the ethanol evaporates. These YEO nanoparticles appear as bright spots in the AAO matrix in Fig. 3e. The mass deposited in the form of particles appears to be less than the mass difference between the overlayer and a thin film. Quantitative analysis of the fluid flow and evaporation is needed to gain further insight into the process.

4.3. Luminescence performance

The photoluminescence of uniform thin films prepared on three different substrates was studied to determine the effects of film thickness and substrate roughness. Regression analysis was used to empirically relate the intensity of the primary emission at 612 nm, I_{612}, to the thickness and RMS surface roughness using the data set shown in the unshaded region in Fig. 1.

$$I_{612}\ (\text{a.u.}) = -19700 + 1320\,t\ (\text{nm}) + 220\ \text{RMS}\ (\text{nm}) \quad (3)$$

This phenomenological relationship suggests that the peak intensity is proportional to both the thickness of the film and the surface roughness. The thickness effect can be understood in terms of the total number of luminescent centers in the film. Assuming the centers are homogeneously distributed throughout the film, the intensity of centers per unit area is proportional to the thickness of the film. This argument must be modified slightly for the films prepared on AAO-Si substrates to account for the additional material deposited inside the AAO pores.

The roughness dependence has been addressed in previous work with YEO films [4, 5]. Fig. 8 is a log-log plot of data from the literature for the photoluminescence vs. surface roughness of YEO films using vapor deposition methods. The data, which span over almost three orders of magnitude of roughness, was collected from papers that separately reported the photoluminescence intensity and surface roughness for films on alumina, silicon and diamond [3, 4, 31]. A single plot was possible because the studies were performed by the same research group and contained internal references to the relative intensities between samples studied in different papers. The photoluminescence-surface roughness relationship has a linear dependence in accordance with Eq. (3).

The intrinsic quantum efficiency of YEO prepared using the templating approach was evaluated using particles. As seen in Table II, the QE of the nanocrystallite particles was about one quarter that of YEO with micron-sized grains. The decrease in relative quantum efficiency has been previously observed in YEO nanoparticles and is explained in terms of the increased number of surface recombination sites present as the surface area to volume ratio increases [2]. This increases the non-radiative energy transition rates for the excited Eu^{3+} center decreasing the QE.

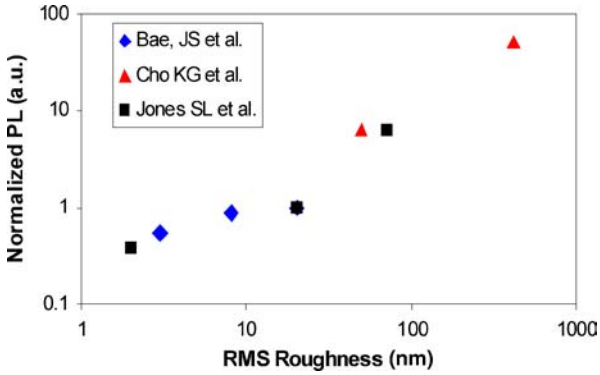

Figure 8 Effects of surface roughness on measured intensity. The results from several papers are plotted on a single graph. The data suggest a linear trend over almost three orders of magnitude.

5. Conclusions

Uniform mesoporous YEO thin films with thicknesses tunable from 100 to 500 nm were synthesized by spin-coating solutions containing block copolymer and yttrium and europium salts. The photoluminescence of the films was proportional to the thickness and surface roughness. Excessive polymer or salt led to inhomogeneities that caused uncontrolled texturing. While the intrinsic QE of nanocrystalline YEO was only 25% that of YEO with micron-sized crystallites, the apparent brightness of films could be increased by spin-coating onto roughened surfaces. The templated synthesis approach is a simple and well-controlled method for the synthesis of YEO thin films for the fabrication of luminescent devices.

Acknowledgements

Part of this work was funded by NIST ATP contract # 70NANB2H3030, "Synthesis platform for Templated Nanostructured Materials". Discussions with R. Corderman and D. S. Williams regarding the synthesis, J. Johnson regarding the modeling of the ellipsometric data, and H. Comanzo, A. Setlur, J. Shiang, and J. Vartuli regarding the luminescence characterization are gratefully acknowledged. We thank J. McKiever for nitrogen adsorption and TGA/DTA measurements, R. Klinger for surface roughness measurements, J. Johnson for assistance with ellipsometric modeling L. Denault for HR-SEM analysis of the films, and R. Nardi and R. Rohling for preparing the aluminum and porous anodic alumina substrates.

References

1. G. BLASSE and B. C. GRABMEIER. Luminescent materials. (Spinger-Verlag, Berlin, 1994).
2. R. SCHMECHEL, M. KENNEDY, H. VON SEGGERN, H. WINKLER, M. KOLBE, R. A. FISCHER, L. XAOMAO, A.

BENKER, M. WINTERER and H. HAHN, *J. Appl. Phys.* **89** (2001) 1679.
3. S. L. JONES, D. KUMAR, R. K. SINGH and P. H. HOLLOWAY, *Appl. Phys. Lett.* **71** (1997) 404.
4. K. G. CHO, D. KUMAR, D. G. LEE, S. L. JONES, P. H. HOLLOWAY and R. K. SINGH, *Appl. Phys. Lett.* **71** (1997) 3335.
5. K. G. CHO, D. KUMAR, P. H. HOLLOWAY and R. K. SINGH, *Appl. Phys. Lett.* **73** (1998) 3058.
6. K. S. SOHN, N. SHIN, Y. C. KIM and Y. R. DO, *Appl. Phys. Lett.* **85** (2004) 55.
7. A. KONRAD, T. FRIES, A. GAHN, F. KUMMER, U. HERR, R. TIDECKS and K. SAMWER, *J. Appl. Phys.* **86** (1999) 3129.
8. B. BIHARI, H. EILERS and B. M. TISSUE, *J. Luminescence* **75** (1997) 1.
9. K. WILLIAMS, H. YUAN and B. M. TISSUE, *J. Luminescence.* **83–84** (1999), 297.
10. K. G. CHO, D. KUMAR, S. L. JONES, D. G. LEE, P. H. HOLLOWAY and R. K. SINGH, *J. Electrochem. Soc.* **145** (1998) 3456.
11. S. J. RHEE, J. O. WHITE, S. LEE and H. CHEN, *J. Appl. Phys.* **90** (2001) 6110.
12. D. K. WILLIAMS, B. BIHARI, B. M. TISSUE and J. M. MCHALE, *J. Phys. Chem. B.* **102** (1998) 916.
13. P. K. SHARMA, M. H. JILAVI, R. NASS and H. SCHMIDT, *J. Lumin.* **82** (1999) 187.
14. T. HIRAI, T. HIRANO and I. KOMASAWA, *J. Mater. Chem.* **10** (2000) 2306.
15. J. A. NELSON, E. L. BRANT and M. J. WAGNER, *Chem. Mater.* **15** (2003) 688.
16. C. WU, W. QIN, G. QIN, D. ZHAO, J. ZHANG, S. HUANG, S. LU, H. LIU and H. LIN, *Appl. Phys. Lett.* **82** (2003) 520.
17. T. KIJIMA, K. IWANAGA, T. HAMASUNA, S. MOHRI, M. YADA, M. SEKITA and M. MACHIDA, *Mat. Res. Soc. Symp. Proc.* **775** (2003) 29.
18. M. YADA, H. KITAMURA, M. MACHIDA and T. KIJIMA, *Inorg. Chem.* **37** (1998) 6470.
19. Y. LU, R. GANGULI, C. A. DREWIEN, M. T. ANDERSON, C. J. BRINKER, W. GONG, Y. GUO, H. SOYEZ, B. DUNN, M. H. HUANG and J. I. ZINK, *Natur.* **389** (1997) 364.
20. P. YANG, D. ZHAO, D. I. MARGOLESE, B. F. CHMELKA and G. D. STUCKY, *Chem. Mater.* **11** (1999) 2813.
21. H. MASUDA, et al., *Appl. Phys. Lett.* **71** (1997) 2770; F. LI, L. ZHANG and R. M. METZGER, *Chem. Mater,* **10** (1998) 2470.
22. C. HIMCINSCHI, M. FRIEDRICH, C. MURRAY, I. STREITER, S. E. SCHULZ, T. GESSNER and D. R. T. ZAHN, *Semiconductor Sci. and Tech.* **16** (2001) 806.
23. T. JÜSTEL, J. C. KRUPA and D. U. WEICHERT, *J. Lumin.* **93** (2001) 179.
24. D. MEYERHOFER, *J. Appl. Phys.* **49** (1978) 3993.
25. J. D. PLUMMER, M. D. DEAL and P. B. GRIFFIN, (Silicon VLSI Technology: Fundamentals, Practice and Modeling). (Prentice Hall, Upper Saddle River, NJ, 2000).
26. G. K. WILLIAMSON and W. M. HALL, *Acta Met.* **1** (1953) 22.
27. N. A. MELOSH, P. LIPIC, F. S. BATES, F. WUDL, G. D. STUCKY, G. H. FREDRICKSON and B. F. CHMELKA, *Macromolecules* **32** (1999) 4332.
28. W. D. KINGERY, H. K. BOWEN and D. R. ULHMANN, "*Introduction to Ceramics*" (John Wiley and Sons, New York, 1960).
29. G. WANKA, H. HOFFMAN and W. ULBRICHT, M*acromolecules* **27** (1994) 4145.
30. Based on the bulk densities, there is a 7% decrease in the volumetric density of yttrium atoms when dense $Y(NO_3)_3{\cdot}6H_2O$ is converted to dense Y_2O_3.
31. J. S. BAE, J. H. JEOUNG, S. YI and J. PARK, *Appl. Phys. Lett,* **82** (2003) 3629.

Received 2 May
and accepted 24 August 2005